Earth and Planetary Science Letters ••• (••••) •••–•••

Contents lists available at ScienceDirect

Earth and Planetary Science Letters

www.elsevier.com/locate/epsl

Arrival-angle anomalies across the USArray Transportable Array

Anna Foster [a,*], Göran Ekström [a], Vala Hjörleifsdóttir [b]

[a] Department of Earth and Environmental Sciences, Columbia University, 61 Route 9W, Palisades, NY 10964, USA
[b] Instituto de Geofisica, Universidad Nacional Autónoma de México, Ciudad Universitaria, Circuito de la Inv. Científica s/n, Coyoacán, C.P. 04510, México D.F., Mexico

ARTICLE INFO

Article history:
Accepted 30 December 2013
Available online xxxx
Editor: P. Shearer

Keywords:
surface wave
USArray
phase velocity
arrival angle
western US

ABSTRACT

We construct composite maps of surface-wave arrival-angle anomalies using clustered earthquakes and an array method for measuring wave-front geometry. This results in observations of arrival angles covering the entire footprint of the USArray Transportable Array during 2006–2010. Bands of arrival-angle deviations in the propagation direction indicate the presence of heterogeneous velocity structure both inside and outside of the array. We compare the observed patterns to arrival angles predicted using two global tomographic models, the mantle model S362ANI and the surface-wave-dispersion model GDM52. We use both ray-theory-based prediction methods and measurements on synthetic data calculated using a spectral-element method. Both models and all prediction methods produce similar mean arrival angles and long-wavelength patterns of anomalies which are similar to the observations. Predicted short-wavelength features generally do not agree with the observations. The spectral-element method produces some complexity that is not obtained using the ray-theory-based methods; this predicted complexity is similar in character to the observed patterns, but does not match them.

1. Introduction

The study of surface waves has revealed significant complexity in the wave field resulting from refraction and scattering across heterogeneous velocity structures (e.g., Masters et al., 1984; Lay and Kanamori, 1985). The resultant deviation from the great-circle path can be measured by the arrival angle, a quantity describing the directionality of the incoming wave. A related quantity is the polarization, a measurement of both the directionality (arrival angle) and the ellipticity of the wave. Arrival-angle anomalies result from the gradient of the velocity structure they cross; the linear approximation of their sensitivity has been described by Woodhouse and Wong (1986), and these and other variations of the equations (e.g., Larson et al., 1998) can be used to predict or invert arrival-angle anomalies.

There are two main ways in which surface-wave arrival angles can be measured: single, three-component-station methods and array-based methods. Within the former group, there exist a variety of time-domain (e.g., Flinn, 1965; Montalbetti and Kanasewich, 1970; Vidale, 1986; Jackson et al., 1991; Larson and Ekström, 2002), spectral (e.g., Lerner-Lam and Park, 1989; Laske et al., 1994), and both time- and frequency-dependent techniques for measuring polarization (e.g., Jurkevics, 1988; Paulssen et al., 1990). Array-based methods are typically some variation of beamforming (e.g., Levshin and Berteussen, 1979; Zywicki and Rix, 2005; Tanimoto and Prindle, 2007; De Cacqueray et al., 2011). This is the approach we take here, using a "mini-array" method that fits the predicted phase from varying backazimuths to observations from a small subset of stations to find the best-fitting arrival angle.

Arrival-angle and polarization measurements are used for a variety of applications. For earthquake source studies, these include the location of earthquakes, especially small magnitude local events (e.g., Ruud et al., 1988; Baker and Stevens, 2004), and identification of Rayleigh waves (and other phases) and subsequent surface-wave magnitude estimation, with application to Nuclear Test Ban verification (e.g., Selby, 2001). Due to their sensitivity to lateral gradients in velocity, arrival-angle anomalies can be used with phase measurements to determine velocity structure. This is particularly valuable for determining small-scale structure (e.g., Laske, 1995; Laske and Masters, 1996; Yoshizawa et al., 1999) and for discriminating between isotropic and anisotropic velocity structure (e.g., Grünewald, 1988; Laske and Masters, 1998; Larson et al., 1998). Additional applications include seismic exploration (e.g., Takahashi, 1995), orienting seismometer components (e.g., Laske, 1995; Larson and Ekström, 2002; Ekström and Busby, 2008), and updating or benchmarking tomographic models based on the arrival-angle predictions from synthetic data (e.g., Larson and Ekström, 2002; Ji et al., 2005).

The first goal of this paper is to demonstrate the robustness and consistent repeatability of arrival-angle observations made using the mini-array method across the USArray. This provides

* Corresponding author.
E-mail addresses: afoster@ldeo.columbia.edu (A. Foster), ekstrom@ldeo.columbia.edu (G. Ekström), vala@geofisica.unam.mx (V. Hjörleifsdóttir).

0012-821X/$ – see front matter
http://dx.doi.org/10.1016/j.epsl.2013.12.046

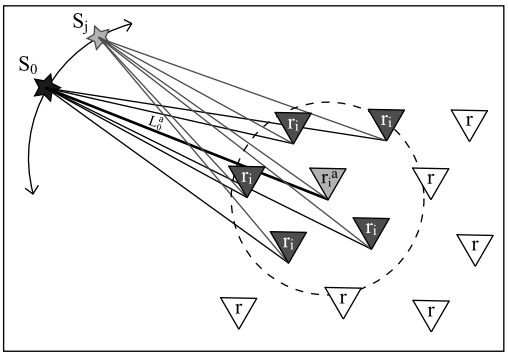

Fig. 1. Illustration of search algorithm to find the best-fit apparent source location (S_j) for a given station (r^a) and source (S_0), using stations r_i that fall within a specified radius. The distance between S_0 and r^a, L_0^a, remains fixed. Figure taken from Foster et al. (2014).

a snapshot of the wave field over the active portion of the array. The second goal is the construction of maps of arrival-angle deviations across the entire footprint of USArray, creating a more comprehensive view of wave propagation across the United States. The third goal is a qualitative characterization of the anomaly patterns and direct comparison with those predicted by current models of global 3-D structure. Because arrival-angle deviations are more sensitive to small-scale structure than typically used phase or travel-time measurements, these observations and comparisons provide a different perspective on wave propagation and model accuracy.

2. Method

The mini-array method used to make arrival-angle estimates in this study requires single-station measurements of phase. We obtain these measurements following Ekström et al. (1997). This method describes a seismogram with a phase, φ, and amplitude, A. A trial fundamental-mode model seismogram u^M is calculated using the source and receiver locations, focal mechanism, and predicted phase and amplitude effects of propagation in a reference Earth model (SH8U4L8; Dziewonski and Woodward, 1992). It is then iteratively matched to the observed surface-wave signal u^S by minimizing the misfit. This is initially performed at long periods, then the passband is progressively expanded to include shorter periods, which, combined with a requirement for surface-wave dispersion curves that vary smoothly with frequency, prevents cycle-skipping. Further details of the single-station method are given by Ekström et al. (1997).

For an array with dense station coverage, we use a small subset of the single-station phase data near the location of interest (a mini array) to estimate the geometry of the wave front and the direction of propagation of the wave near each station. Details of the method are presented in Foster et al. (2014); here, we provide a short summary.

To estimate the arrival angle α^a at a station r^a at a specified period, we select all N receivers, r_i, within some radius of station r^a. We require a minimum number of stations within the mini array to make the measurement. We vary the apparent source location along an arc, fixing the epicentral distance from r^a (Fig. 1). This effectively varies the arrival angle at station r^a. For each trial source location S_j^a, we consider the difference in phase between each station r_i and station r^a to be due to the inter-station distance divided by a local phase velocity c_j^a, plus an unknown phase offset at r^a. We solve for the local phase velocity c_j^a in the least-squares sense. This results in a misfit between predicted and observed phase associated with each trial source location S_j^a. We select the trial source location with the smallest misfit to be the best-fit apparent source location S_*^a, which corresponds to the best-fit arrival angle at station r^a, α_*^a. The difference between the arrival angle and the backazimuth to S_*^a is the arrival-angle anomaly. This process is repeated for all stations for a selected event.

3. Data

We use data recorded on the USArray Transportable Array (TA) from January 2006 to December 2010. A key component of the TA program is its "rolling" nature; the array aims to cover the continental United States uniformly with 70-km grid spacing, but does so in installments (www.usarray.org). We therefore use events recorded on an evolving array that, in aggregate, covers the area between 93°–125°W longitude and 25°–50°N latitude. We consider all events greater than magnitude 5.5, with focal depths less than 50 km and epicentral distances in the range of 10°–165°. The examples chosen for this paper were primarily selected for the large number of high-quality single-station measurements (300–400) that could be made for each event.

4. Observations

We apply the mini-array arrival-angle measurement method to the TA data set of single-station measurements. We select a radius of 1° for the mini array; this size is small enough to observe small-scale patterns, while being large enough to encompass several stations and ensure a good measurement. We require a minimum of 3 stations to make an arrival-angle estimate, with most mini-array measurements using 7–8 stations. Some measurements include as many as 12 stations. Previous studies have observed surface-wave arrival-angle anomalies of up to 15° (Lerner-Lam and Park, 1989) and 5°–30° (Laske et al., 1994) in the period range used here, 25–100 s. We limit our grid search to arrival-angle anomalies of ±15°, to avoid the effects of very small-scale complexity and spurious measurements. We find that most observed deviations fall within this range.

An example of arrival-angle anomaly measurements for a single event can be seen in Fig. 2. Positive values indicate clockwise rotation from the great-circle path; negative values indicate counter-clockwise rotation. Some characteristics of the pattern are consistent for all events: as the wave field moves across the array, arrival angles are generally coherent in the propagation direction. This results in the banded appearance of the anomalies. Comparing arrival-angle deviations with contours of the single-station phase measurements for the same event (Fig. 2), it is clear that the variations in the anomalies correspond to variations in the wave front, with arrival-angle anomalies of zero aligning more or less with peaks or valleys in the contours. Arrival angles thus provide a useful way to characterize the wave-front propagation quantitatively.

The effects of wavelength and depth sensitivity are evident when comparing measurements made at different periods (Fig. 3). Although at all periods, the arrival-angle anomalies span the allowed range from −15° to +15°, anomalies are larger at short periods. At 25–35 s, Rayleigh waves have significant sensitivity to crustal structure. This is reflected in the complex patterns observed. At 50 s, there is less sensitivity to the crust, and the anomaly pattern is simpler. The width of the bands increases, reflecting both increasing wavelength and what we expect to be the expression of smoother mantle structure. By 100 s, the pattern is relatively simple and should be predominantly a result of mantle structure.

For this paper, we choose to focus on only 50-s Rayleigh wave results. This allows us to see strong and interesting patterns in the arrival-angle anomalies across the array, without some of the complicating effects of the heterogeneous crust, though we will show that crustal structure is still important. Additionally, most current

Please cite this article in press as: Foster, A., et al. Arrival-angle anomalies across the USArray Transportable Array. Earth Planet. Sci. Lett. (2014), http://dx.doi.org/10.1016/j.epsl.2013.12.046

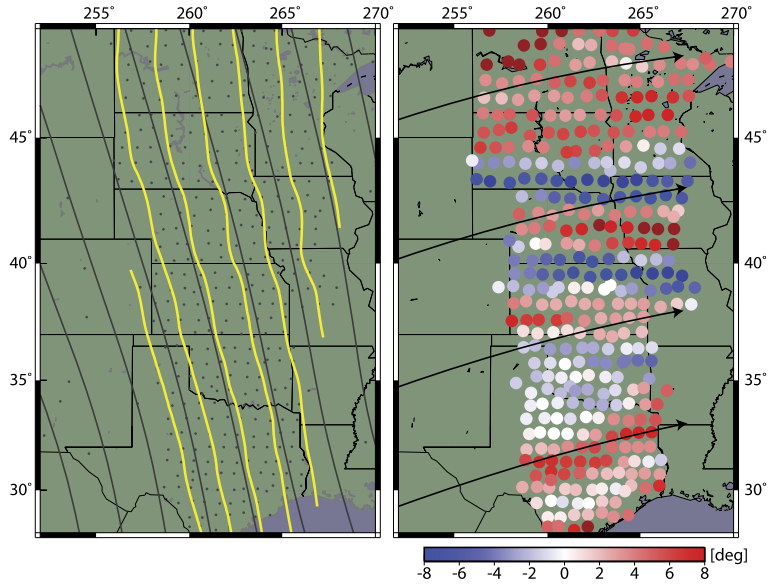

Fig. 2. Left: Contours of single-station phase measurements (yellow lines) at all stations (black dots) recording an event located at 19.65°S, 168.10°E near Vanuatu Islands. Phase increases from west–southwest to east–northeast. Black lines show spherical wave fronts. Right: Example of mini-array arrival-angle anomaly estimates for the same event, using a mini-array of 1° radius. Red shows angles clockwise from the great-circle-path arrival, indicated by the black lines; blue shows counter-clockwise arrivals. Both figures calculated for Rayleigh waves at 50 s period. (For interpretation of the references to color in this figure legend, the reader is referred to the web version of this article.)

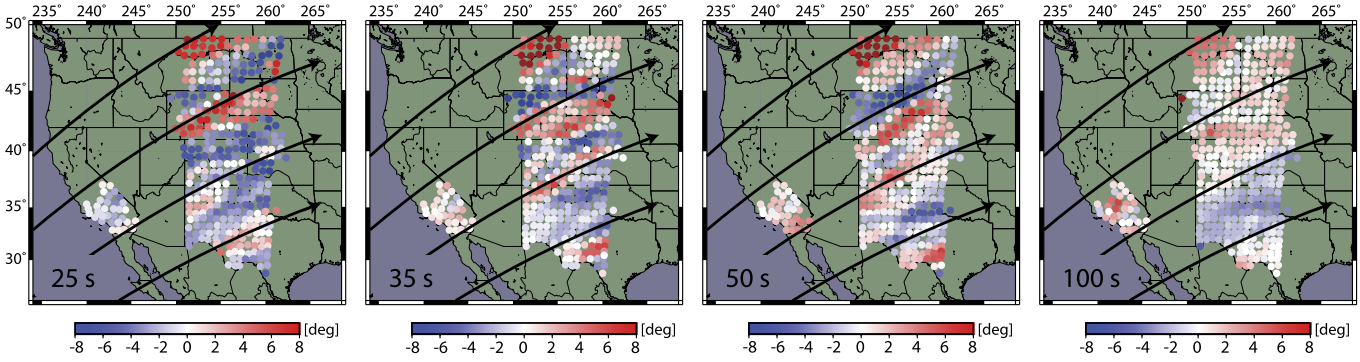

Fig. 3. Arrival-angle anomaly estimates for Rayleigh waves at 25, 35, 50, and 100 s period, for an event located at 16.45°S, 173.06°W near Samoa. The source is approximately 85° away, with a backazimuth of 243°. Black lines indicate the direction of wave propagation along the great-circle path.

tomographic models do not include detailed shallow crustal structure, and 50-s Rayleigh waves will provide a better comparison with predictions from these models.

5. Composite maps

Observations of the arrival angle for an individual event show a range of different patterns, as well as variations within these patterns as the waves progress across the array. The TA is designed to cover the entire contiguous United States, providing a unique opportunity to observe wave-field behavior at a large scale. However, due to its rolling nature, measurements from any single event only cover a portion of the potential area. Compounding this, we cannot often make measurements for all stations in the TA for a given earthquake. The maximum number of stations at which we have measurements for a single earthquake is 436, but the average is 156. We wish to combine the observations from several events, here termed "constituent" events, with similar source locations that occur over the course of the TA lifetime, to take full advantage of the coverage of the array. This would result in a "composite" figure showing arrival-angle anomaly observations for a source location over the extent of the TA study region. In the following sections, we demonstrate the feasibility of this approach and show results for several composite examples.

5.1. Event consistency and selection

The primary requirement for compiling results into composite figures is that observations are repeatable; that is, for similar events, we produce similar arrival-angle anomaly measurements on the same stations. We test this by comparing results for two earthquakes (Fig. 4). The two earthquakes are separated in CMT location by 17 km, and in time by 9 days. 383 arrival-angle measurements were made for the event shown in Fig. 4a, and 401 measurements for the event in Fig. 4b. The results are nearly identical, with a correlation between the measured arrival angles of 95% for the 375 overlapping stations, indicating good repeatability.

Such close pairs of events with nearly identical source locations are relatively rare, and therefore we cannot limit constituent events to this category. Examining large groups of events within a 5° radius, we find that the range within which the arrival-angle observations are consistent varies. In many cases, events separated by 3°–4° are consistent. However, for certain source areas, events separated by as little as 2° show variations in the arrival-angle

Please cite this article in press as: Foster, A., et al. Arrival-angle anomalies across the USArray Transportable Array. Earth Planet. Sci. Lett. (2014), http://dx.doi.org/10.1016/j.epsl.2013.12.046

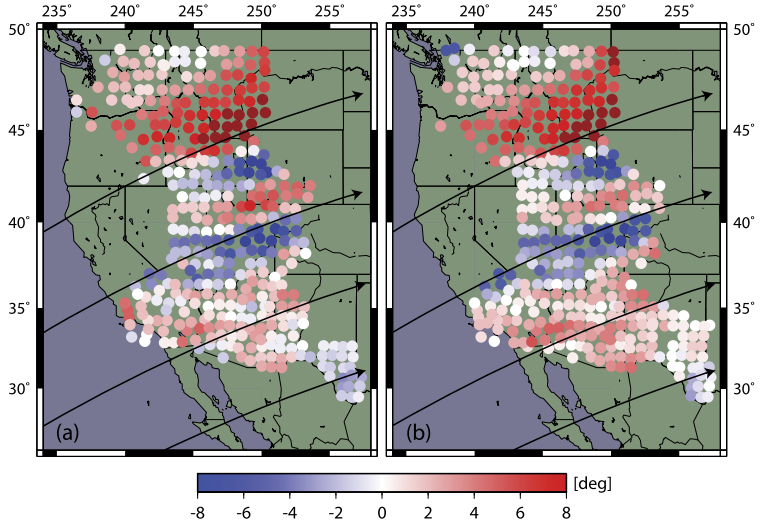

Fig. 4. Example of arrival-angle anomaly observations from two events used in the construction of a composite map. The events are located at (a) 20.36°S, 168.72°E, and (b) 20.23°S, 168.81°E, and the results have a correlation of 95%. Black lines indicate the direction of wave propagation along the great-circle path.

pattern. We therefore use a combination of proximity in earthquake source, correlation of arrival-angle deviations from events that were recorded on overlapping array configurations, and visual inspection to select constituent events. We find that source mechanism has no discernible effect on the pattern of anomalies for most events.

The remaining task for making composite figures is to find a source location with earthquakes meeting the above criteria, as well as having a reasonable distribution throughout the time period. This can be challenging, as even regions with high earthquake occurrence rates often experience quiescent periods. However, many locations do satisfy all the above criteria, particularly in the southwest Pacific. We compile all arrival-angle observations for constituent earthquakes, and average anomalies for stations with multiple observations.

5.2. Results

We have constructed 10 composite maps using the above-mentioned criteria. Constituent events typically have correlation values between measured arrival-angle anomalies for overlapping events of 80% or better. We have selected four examples to present here; locations and focal mechanisms of the central event (in color) and all constituent events (in grey) are shown in Fig. 5. Composite observations are shown in Fig. 6.

Loyalty Islands (Fig. 6a): This composite figure uses 25 earthquakes, all located within 2° of the central event (colored focal mechanism in Fig. 5a). The earthquakes span the time period March 2007 to December 2010. This provides measurements of 1108 unique stations, covering nearly the entire study area. The source location is approximately 100° away from the center of the array, with a backazimuth of approximately 252°.

Arrival-angle deviations for this composite figure range from −14° to 15°. Bands of positive and negative anomalies, aligned roughly with the great-circle ray paths shown in black, are the dominant signal. For this event, wave-field propagation exhibits a range of behaviors. In the northernmost part of the study area, a wide band of strongly positive angles is very linear, and trending east–northeast. Immediately below is a narrower band of negative angles trending due east. Looking further south in the study area, the bands remain narrow, less than 2° wide, and exhibit considerable curvature. Most of the bands begin at the edge and remain fairly uniform across the array, indicating that the arrival-angle anomalies originated outside of the array.

Tonga Islands (Fig. 6b): This figure is a compilation of 19 earthquakes, all within a radius of 0.9° (Fig. 5b). Constituent earthquakes span the time period February 2006 through December 2010, covering 1063 unique stations. The source area is at a distance of approximately 83° from the array, with a backazimuth of approximately 244°.

The great-circle path from the source area to the array is similar to that of the Loyalty Islands composite figure; despite this, the two events have very different arrival-angle anomaly patterns. For this composite figure, the arrival angles generally show smaller deviations from the great-circle path, ranging from −11° to 12°. As for the Loyalty Islands, the northernmost band is wide and strongly positive, and the southern bands are narrower; however, all of the bands are linear and most of them have increasing deviations as the wave front progresses from southwest to northeast. Some are not even distinguishable as they enter the array at the west coast, which could indicate that they are due to heterogeneous structure within the array. The lack of strong anomalies at the western edge of the array may be due to the 90° incidence of the wave field on the ocean–continent boundary for this source area.

North of Ascension Island (Fig. 6c): This composite figure uses only 4 earthquakes, with the farthest being 1.4° from the central event (Fig. 5c). The constituent earthquakes span the time period February 2006 through November 2008, covering only 607 unique stations. The source area is at a distance of approximately 91° from the array, with a backazimuth of approximately 90°. This composite highlights the difficulty of finding suitable groups of events outside of the Pacific ring. Although the data do not cover the entire study region, they provide a valuable snapshot of wave propagation from the east, as well as evidence that composite figures do not require large amounts of averaging to produce robust patterns.

In comparison with the previous two composite figures, the bands of anomalies from this source area are wider, and more negative. Arrival-angle deviations range from −15° to 8.25°. Bands parallel the great-circle ray paths in the north, but are rotated clockwise in the south. Two negative bands appear to be joining up at 38°N, 115°W.

Easter Island (Fig. 6d): This figure is made up of results from 8 earthquakes within a radius of 1.6° (Fig. 5d). Constituent earthquakes span the time period November 2006 through September 2009, yielding results at 838 unique stations. The source area is at a distance of approximately 69° from the center of the array, with a backazimuth of approximately 186°.

Please cite this article in press as: Foster, A., et al. Arrival-angle anomalies across the USArray Transportable Array. Earth Planet. Sci. Lett. (2014), http://dx.doi.org/10.1016/j.epsl.2013.12.046

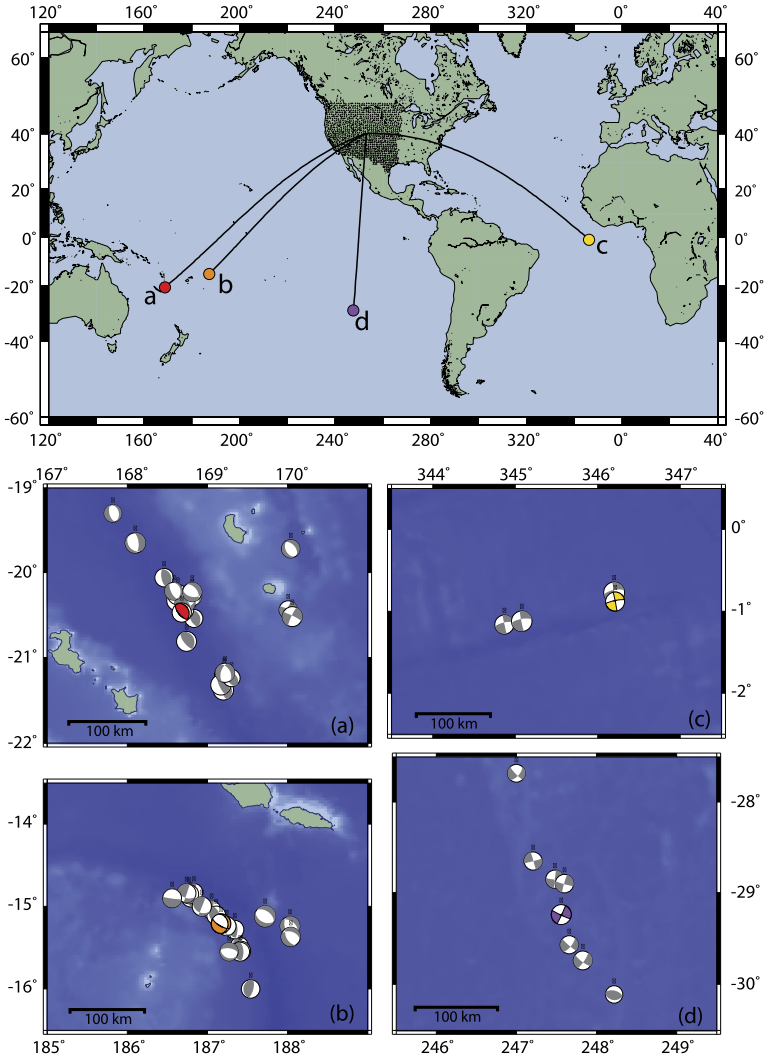

Fig. 5. Top: Location map. All USArray TA stations for the time period 2006–2010 shown with black triangles. Source location area for the four example composite arrival-angle anomaly observations (Fig. 6) shown by colored circles, with great-circle ray paths in black. Labels and colors correspond to the detailed maps at bottom, showing locations and focal mechanisms for the constituent events of composite figures from the following source areas: (a) Loyalty Islands, (b) Tonga Islands, (c) north of Ascension Island, and (d) Easter Island. Colored focal mechanism signifies the central event used in the calculation of synthetics. (For interpretation of the references to color in this figure, the reader is referred to the web version of this article.)

Because the source area is directly south of USArray, we largely observe the effects of interaction with the Mexican coastline in this example. As the wave field enters the array, arrival-angle anomalies are all positive, except for the easternmost stations in Texas. As the wave field moves northward, bands of positive and negative angles appear, ranging from −14.5° to 14°. These bands are very well aligned with the great-circle ray paths. The bands are 3°–5° wide, wider than most of the bands in the previous examples.

These examples illustrate the range of patterns that can be observed in the composite maps. Banded patterns may have short (2°) or long (5°) wavelengths. They may be linear or curved, and parallel the great-circle ray path or deviate from it. Additionally, the arrival-angle anomalies may most commonly be observed to originate outside the array, but some anomalies appear to be a result of heterogeneity within the array.

6. Testing current tomographic models

We use the arrival-angle observations as a metric for evaluating current velocity models. We focus on global models, since we infer that many anomalies result from structure outside of the array. In this section, we describe the velocity models used and the methods for predicting arrival-angle values, and present a comparison of the observations and model predictions.

6.1. Models

6.1.1. S362ANI

The radially anisotropic mantle model S362ANI (Kustowski et al., 2008) was derived using a large data set of multiple data types to ensure sensitivity at all mantle depths. The model was parameterized using 362 spherical splines to define lateral variations in shear-wave velocity, radial anisotropy, and topography of discontinuities. Sixteen B-splines, split at 650 km depth, describe isotropic velocity variations in the radial direction. The nominal lateral resolution of the model is 1000 km. We make waveform predictions using the full 3-D model combined with the 2°-by-2° crustal model CRUST2.0 (Bassin et al., 2000). We also use phase-velocity maps derived from S362ANI with CRUST2.0 to predict surface-wave travel times and arrival angles. One version of the phase-velocity maps is expanded in spherical harmonics up to degree 40, resulting in smooth structure suitable for ray tracing. The other version of the maps is defined on 2°-by-2° pixels, and expresses the full heterogeneity of CRUST2.0, making it comparable

Please cite this article in press as: Foster, A., et al. Arrival-angle anomalies across the USArray Transportable Array. Earth Planet. Sci. Lett. (2014), http://dx.doi.org/10.1016/j.epsl.2013.12.046

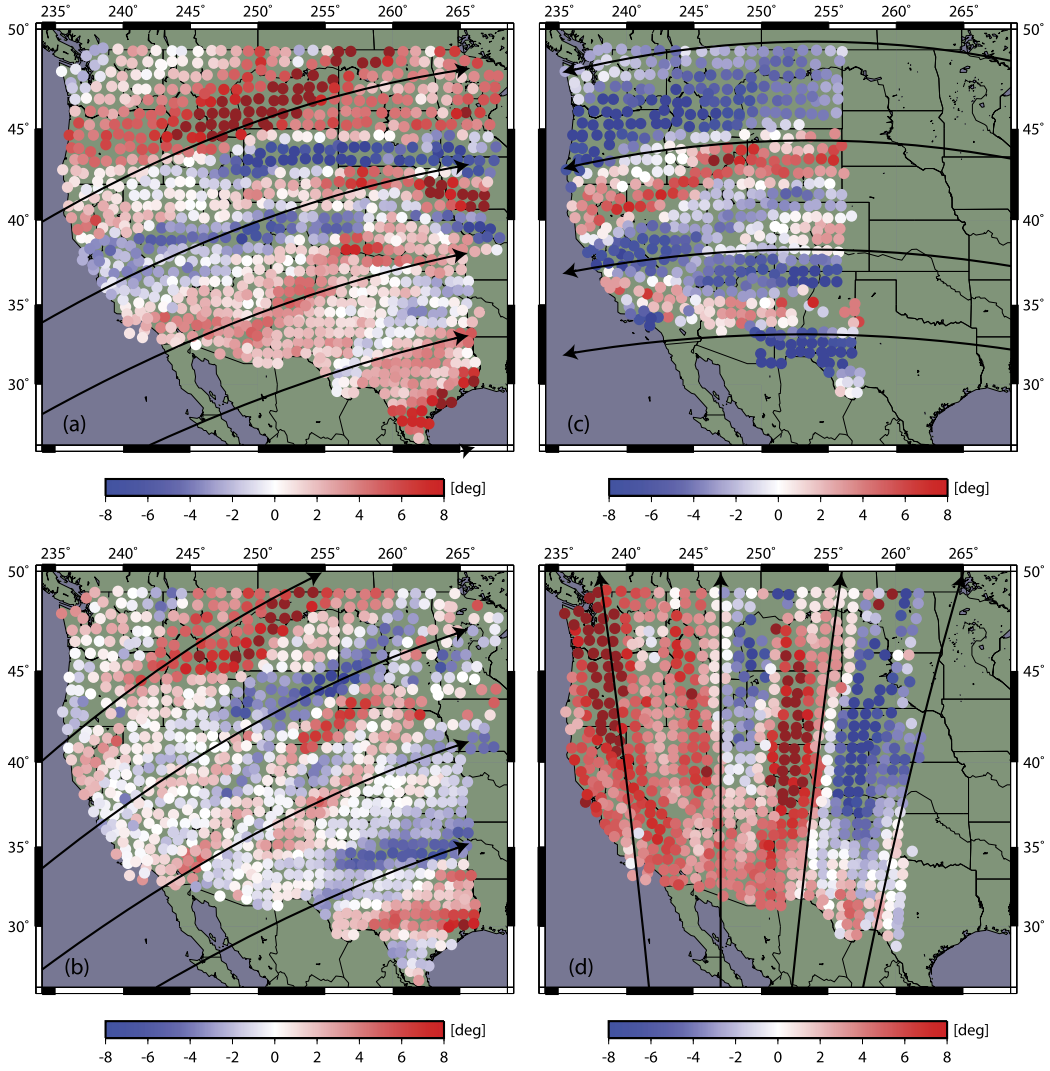

Fig. 6. Composite arrival-angle anomaly observations for four source areas, in (a) Loyalty Islands, (b) Tonga Islands, (c) north of Ascension Island, and (d) Easter Island. Constituent event locations are shown in Fig. 5. Arrival-angle anomaly estimates are averaged at each station location. Black lines indicate the direction of wave propagation along the great-circle path. For further details of the composite observations, see the text.

to the model used in the numerical waveform predictions. In all cases, sediments are accounted for by including sediment thicker than 2 km.

6.1.2. GDM52

Global Dispersion Model GDM52 (Ekström, 2011) describes the Love and Rayleigh wave isotropic phase-velocity dispersion between 25–250 s, as well as the azimuthally anisotropic Rayleigh wave dispersion. A large number of earthquake phase-anomaly measurements, recorded at global stations, were inverted using a ray-theoretical framework. The model was parameterized horizontally with 1442 spherical splines and in frequency with 12 B-splines. The resulting nominal lateral resolution is 650 km. In this study, we use both the anisotropic model and the isotropic portion only to predict arrival angles.

6.2. Prediction methods

6.2.1. Great-circle path predictions

For a given earthquake and receiver, we calculate the predicted phase by integrating along the connecting great-circle path through a phase-velocity model. The result is a single-station phase prediction. We make arrival-angle measurements on the predicted data using the mini-array method. In this study, we make predictions for the smooth and pixel-based isotropic phase-velocity maps derived from 3-D model S362ANI and CRUST2.0, and for the azimuthally anisotropic global phase-velocity model GDM52, and an isotropic version of GDM52. We note great-circle path integration may not be appropriate for use with such small-scale heterogeneities as are contained in the pixel-based phase-velocity map, and it is used here only as a demonstration of the possible anomalies resulting from small-scale structure.

6.2.2. Ray tracing

We use the exact ray-tracing algorithm presented in Larson et al. (1998). Given an isotropic or anisotropic phase-velocity model, this method predicts the phase, arrival angle, and amplitude for a specified source and receiver location.The dynamical ray-tracing equations are derived from the surface-wave dispersion relation in an anisotropic Earth model. We perform ray-tracing through the smooth phase-velocity maps of S362ANI and GDM52. For this approach, both models are azimuthally isotropic. The output of this method is a direct prediction of the arrival angle.

6.2.3. SPECFEM3D Globe

SPECFEM3D Globe is a freely available software package initially developed by Komatitsch and Vilotte (1998) and Komatitsch and Tromp (2002a, 2002b), and further developed and maintained

Please cite this article in press as: Foster, A., et al. Arrival-angle anomalies across the USArray Transportable Array. Earth Planet. Sci. Lett. (2014), http://dx.doi.org/10.1016/j.epsl.2013.12.046

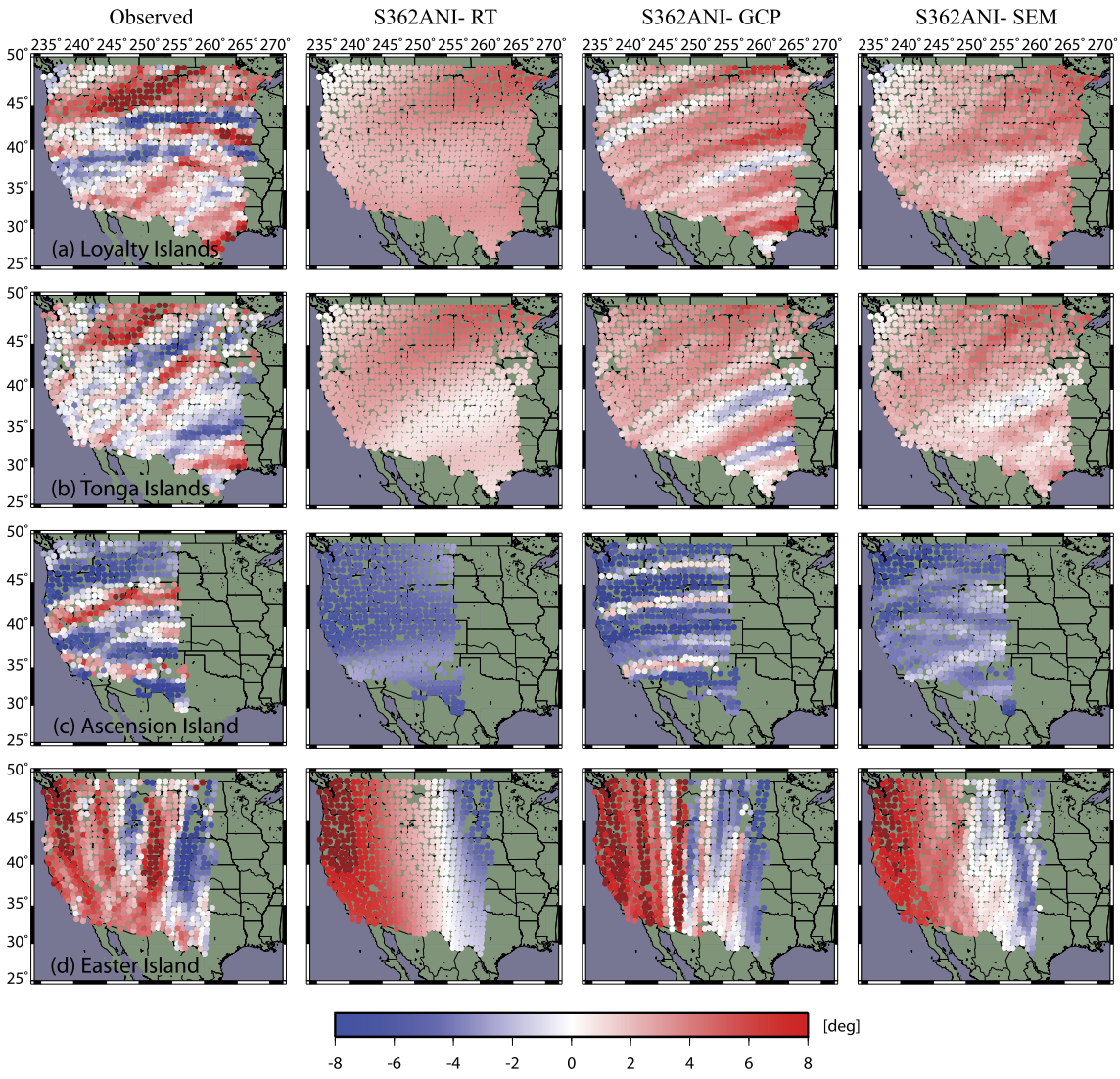

Fig. 7. Comparison of observed composite arrival-angle anomaly maps, as in Fig. 6, for source locations in (a) Loyalty Islands, (b) Tonga Islands, (c) north of Ascension Island, and (d) Easter Island, with predictions from model S362ANI. Model CRUST2.0 and sediments thicker than 2 km were also included. Predictions were made using exact ray tracing through a smooth phase-velocity map (RT, second column), great-circle-path phase integration through a pixel-based phase-velocity map (GCP, third column), and SPECFEM3D Globe with the full 3-D model (SEM, fourth column).

through combined efforts with many others (e.g., Tromp et al., 2010; Peter et al., 2011). This spectral finite-element method calculates seismic wave propagation in a fully 3-D Earth model. It includes effects due to lateral variations in compressional-wave speed, shear-wave speed, density, a 3-D crustal model, ellipticity, topography and bathymetry, the oceans, rotation, and self-gravitation. A point source is applied at the earthquake source location, and the weak form of the wave equation is then solved for displacement at nodes in the mantle and inner core and in terms of the scalar potential in the liquid outer core. The output of this method is a synthetic waveform for each designated station location, which can be convolved with the desired source function.

In this study, we use models S362ANI and CRUST2.0 (Bassin et al., 2000), all available propagation effects (ellipticity, topography, etc.), with 5 processors and 240 surface elements for one chunk, allowing the resulting waveform to be accurate down to a period of approximately 18 s. The CMT solution for each earthquake is obtained from the Global CMT catalog (Dziewonski et al., 1981; Ekström et al., 2012). We make single-station phase measurements on the waveforms followed by mini-array arrival-angle estimates, in the same manner as with the TA data.

6.3. Comparisons

6.3.1. S362ANI

Predictions of arrival-angle anomalies from model S362ANI generally match the average direction of banding and the average sign of the observed arrival-angle anomalies (Fig. 7). The magnitude of the arrival-angle anomalies is under-predicted by ray tracing through the smooth degree-40 phase-velocity map and by SPECFEM for events in the southwest Pacific (Fig. 7a, b), but is very similar for the observed and predicted anomalies from events to the south and east (Fig. 7c, d). Ray tracing produces anomalies that are very smooth, with a band width of approximately 5°–12°. Great-circle path integration through the smooth degree-40 map (not shown) produces anomalies very similar to the ray-tracing results. Great-circle path integration through the pixel-based phase-velocity map produces narrowly banded anomalies with similar magnitudes to the observations. Measurements made on the SPECFEM synthetic seismograms more closely resemble

Please cite this article in press as: Foster, A., et al. Arrival-angle anomalies across the USArray Transportable Array. Earth Planet. Sci. Lett. (2014), http://dx.doi.org/10.1016/j.epsl.2013.12.046

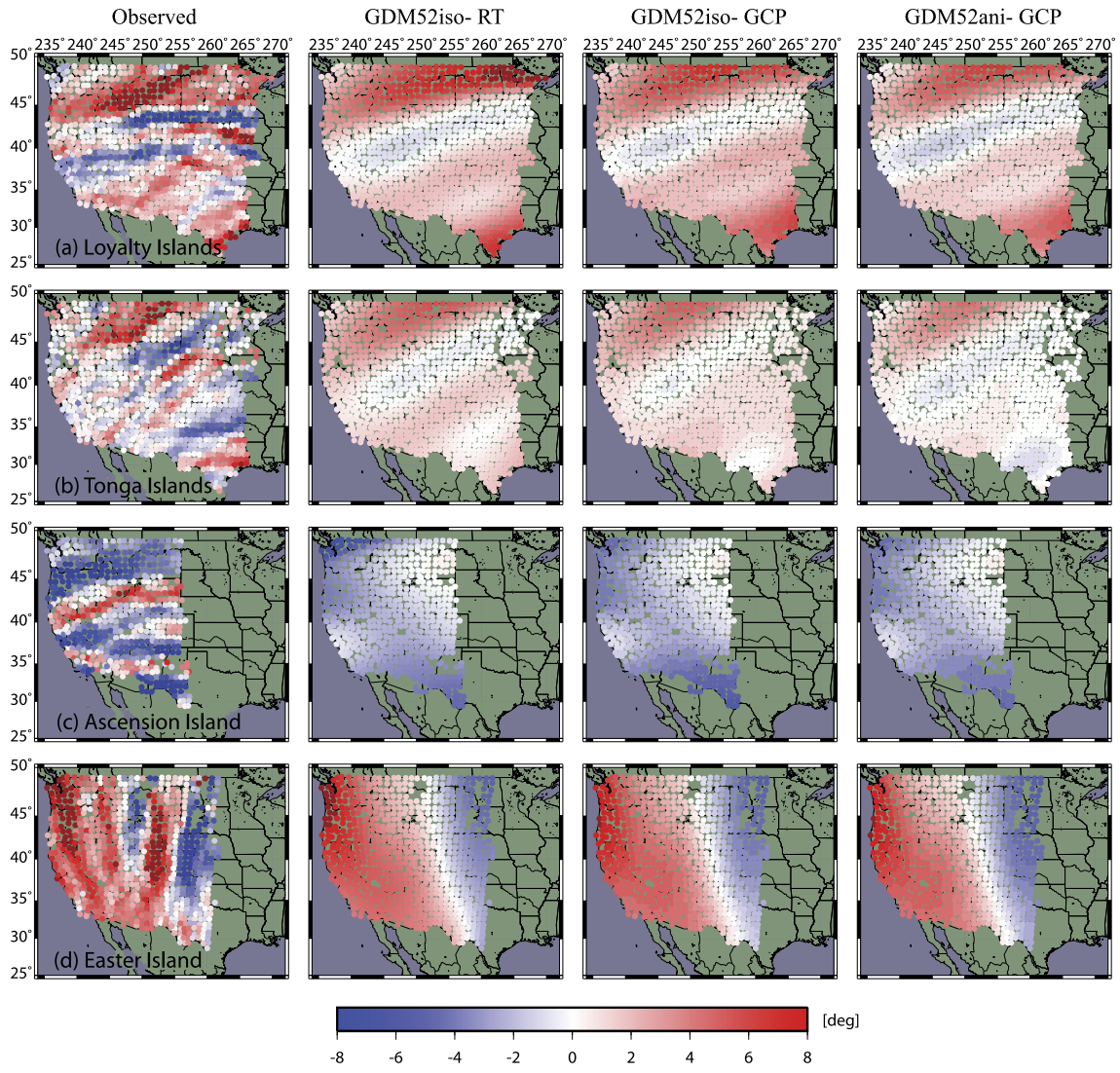

Fig. 8. Comparison of observed composite arrival-angle anomaly maps, as in Fig. 6, for source locations in (a) Loyalty Islands, (b) Tonga Islands, (c) north of Ascension Island, and (d) Easter Island, with predictions from model GDM52. Predictions were made using exact ray tracing with the isotropic portion of the model (RT, second column), great-circle-path phase integration with the isotropic portion of the model (GCP, third column), and great-circle-path phase integration with the full anisotropic model (GCP, fourth column).

the observed band widths and complexity. Correlations between the predicted arrival-angle anomalies from all methods range between 70–99%, except for great-circle path integration through the pixel-based model, which has correlation values of 30–80% with the other results.

6.3.2. GDM52

Predictions from GDM52 using great-circle-path integration and ray tracing are shown in Fig. 8, for both the anisotropic and isotropic versions of the model. In comparison with predictions from the smooth phase-velocity maps of S362ANI, predictions of arrival angles from model GDM52 show an improved match to the observations from events in the southwest Pacific (Fig. 8a, b), in both sign and magnitude of the deviations. Predictions from the southern event (Fig. 8d) are similar to predictions from S362ANI. Predictions from the event located to the east (Fig. 8c), however, do not match the average banding direction, although the average sign is correct. The differences between the predictions from the isotropic and the azimuthally anisotropic models are of the same order as the differences resulting from the great-circle-path integration and ray-tracing prediction methods. Correlations between the predicted arrival-angle anomalies from all methods and models range between 90 and 99%.

7. Discussion

7.1. Composite maps

The construction of the composite maps of arrival-angle anomalies provides a novel way to view the regional wave field across the western half of the United States. The USArray TA is a unique type of seismic installation at present. However, these composite maps can be made for any similarly “rolling” array, or an array that has varied in size over time. Similar techniques could likely be used for other types of observations as well.

Our observation that measurements from small clusters of earthquakes can be combined into a coherent pattern is evidence for smoothly varying velocity structure. The scale over which this is true, however, depends on the region; it is apparent that these patterns are not coherent for earthquakes that differ in location by more than a few degrees. This indicates that short-wavelength (2°–4°) velocity heterogeneity is important for 50-s Rayleigh waves.

Please cite this article in press as: Foster, A., et al. Arrival-angle anomalies across the USArray Transportable Array. Earth Planet. Sci. Lett. (2014), http://dx.doi.org/10.1016/j.epsl.2013.12.046

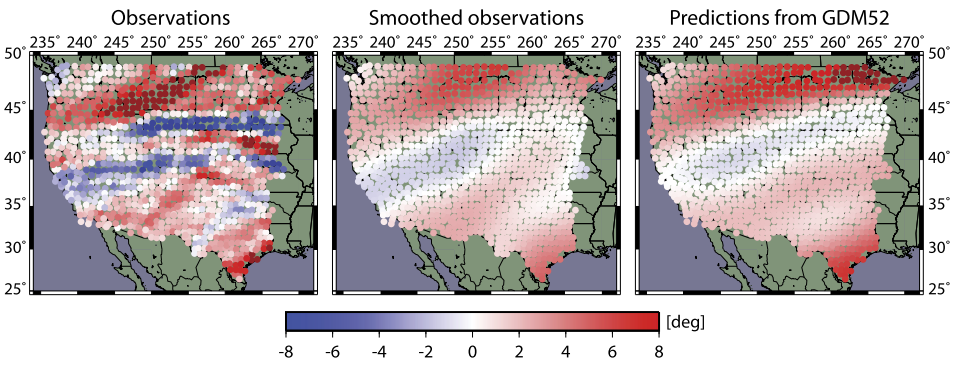

Fig. 9. The observed composite arrival-angle anomaly map for the source location in the Loyalty Islands (Fig. 6a), left, is shown next to the smoothed observations, center. The observations are smoothed using a Gaussian function with a full width at half maximum of 4.7°. The long-wavelength pattern is compared with ray-tracing predictions from model GDM52, right.

Additional information about the distribution of this heterogeneity can be inferred from the observed patterns. Many bands of anomalies clearly are well-developed at the edge of the array, indicating an origin from structure outside the array. This is consistent with observations from Bungum and Capon (1974) and Levshin and Berteussen (1979) associating most refraction with continental boundaries. Structure inside the array creates additional deviations, indicated by bands of anomalies that begin or grow as the wave front progresses. One example of this can be seen in the two southwest Pacific events (Fig. 6a, b). A strong positive anomaly to the north and a strong negative anomaly just south of the first both originate near 43°N, 115°W. This pattern is consistent with the expected deviations resulting from the slow velocities associated with the Snake River Plain and Yellowstone Hotspot (e.g., Lin and Ritzwoller, 2011) as the wave front crossing the anomaly is delayed. A second example can be seen in the Easter Island event (Fig. 6d), where the band of negative anomalies that begins at roughly 33°N, 103°W may be associated with the fast velocities of the Great Plains and southern Rocky Mountains.

7.2. Effect of model structure

Based on the model predictions, then, the wavelength of heterogeneity included in a given model impacts the ability of that model to predict arrival angles. Exact ray-tracing predictions from model S362ANI (Fig. 7, column 2) and from GDM52 (Fig. 8, column 2) are both much smoother than the observed patterns. For events in the southwest Pacific, predictions from the dispersion model GDM52 are more similar to the observations, and, interestingly, smoothing the observed arrival-angle anomalies with a Gaussian function with a full width at half maximum of 4.7° results in a pattern that is strikingly similar to the predictions from GDM52, as shown in Fig. 9.

For all composite maps, correlation values for the predicted and observed arrival-angle deviations from S362ANI are typically low, but positive (5–30%). Correlations are lowest for measurements on SPECFEM synthetic data and predictions from the pixel-based phase-velocity map, likely because of the short-wavelength patterns that resemble the observations, but do not match them. Correlations between observed deviations and those predicted from GDM52 are higher (30–50%). After smoothing the observations as described above, the correlations of anomalies with predictions from S362ANI increase to 5–70%, and the correlations with predictions from GDM52 increase to 50–90%.

The inclusion of the anisotropic structure in GDM52 has a small but noticeable effect on the predicted arrival angles (Fig. 8, columns 3 and 4). It improves the predicted mean arrival-angle anomaly for the composites, typically bringing it to within 0.3° of the observed mean value. Means from predictions from the isotropic version of GDM52 are typically within 1.0° of the observed mean value. Mean arrival-angle anomaly values for predictions from S362ANI differ from the observed mean value by up to 2.3°.

Finally, the complicated effects of shorter-wavelength structure are illustrated in the comparison of the predictions from ray tracing through the smooth phase-velocity maps of S362ANI and CRUST2.0 with the predictions from great-circle path integration through the pixel-based phase-velocity maps from the same models, and the predictions based on the numerical waveforms (Fig. 7). The latter two models retain all of the short-wavelength heterogeneity of CRUST2.0. The pattern resulting from the pixel-based model predictions has very narrow bands of anomalies. These anomalies do not match the overall observed anomaly patterns, but do strongly resemble them. This appears to indicate that crustal structure at the scale included in CRUST2.0 is important for predicting arrival angles at small scales; however, this same structure is included in the model used to make waveform predictions, and does not produce the same strong narrow bands of anomalies with this more accurate prediction method. This indicates that current models of small-scale velocity structure require modifications to produce better predictions of arrival-angle anomalies.

7.3. Limitations of prediction methods

Model predictions made using great-circle-path phase integration and ray tracing typically capture the general character of the arrival-angle anomaly observations, though not their complexity or range of deviations. In contrast, measurements made on synthetic data calculated using SPECFEM have the same type of complexity as the observed measurements, though not the exact details of the pattern. This indicates that ray-theory-based prediction methods are not adequate to explain the small-scale intricacies of the wave field, and are likely not the best choice for including arrival-angle anomaly measurements for applications such as improving tomographic models. This is not a new problem, as Laske and Masters (1996) pointed out that as models include higher-order structure, great-circle approximations and ray tracing may both be inadequate for shorter-period predictions. As mentioned in Section 7.2, this is illustrated by the differences in the predictions based on the great-circle path integration of the pixel model of S362ANI with CRUST2.0 and those based on the synthetic waveforms calculated for the same model.

On the other hand, predictions from great-circle-path integration of phase, ray tracing, and measurements from SPECFEM synthetics are remarkably similar in the large-scale patterns (Fig. 7). The predictions from SPECFEM synthetics appear to be a smoother version of the great-circle path predictions from the pixel-based phase-velocity map, perhaps due to wave-front healing and interference effects that are not accounted for in the integration

Please cite this article in press as: Foster, A., et al. Arrival-angle anomalies across the USArray Transportable Array. Earth Planet. Sci. Lett. (2014), http://dx.doi.org/10.1016/j.epsl.2013.12.046

method. The ray-tracing and great-circle path predictions from the smooth phase-velocity map appear to be a smoother version of the predictions from the SPECFEM synthetics. The mean predicted arrival-angle deviations for the composite maps from each method are typically within 0.5°, and the predicted arrival-angle anomaly maps typically have correlations of 80–95% with each other, with the exception of the predictions from the pixel-based map. These large-scale similarities indicate that ray-theory-based methods are adequate for applications in which the wavelength of heterogeneity of interest is long relative to the surface-wave wavelength.

The measurements made using synthetic data from SPECFEM3D Globe allow us to infer better which limitations result from the methods and which from the models. Due to requirements of smooth gradients in the model, the ray-tracing method cannot predict short-wavelength anomalies that might result from strong crustal heterogeneity, for example. Great-circle-path integration can be used with more heterogeneous models so long as the size of the heterogeneity is long compared to the wavelength, though it lacks some of the wave propagation effects we know to be important. These effects, included in SPECFEM, result in the complex character of the banding that can be observed in the predicted arrival-angle anomaly patterns. However, comparisons to the measurements on synthetic data show that these ray-theoretical methods can predict anomalies at a scale of roughly 5° or more. The discrepancies between observations and predictions at long wavelengths, as in Fig. 9, are therefore attributable to the models. This type of comparison highlights areas in which future models could be improved, in order to predict wave propagation in a heterogeneous Earth more accurately.

8. Conclusions

On a large and regular array such as the Transportable Array, arrival angles can be systematically measured using the mini-array technique. Arrival-angle anomalies are very sensitive to source location. For earthquakes within a source area of roughly 2° radius, consistent arrival-angle anomaly patterns are produced; beyond this, velocity heterogeneity results in very different patterns. Using the observations from earthquakes within the same source region, measured anomalies can be combined into composite figures that describe the wave field over a larger area.

The resulting maps provide a snapshot of wave propagation across the array. Many of the large-scale bands of arrival-angle deviations appear to result from structure outside of the array. Much of the complexity in the wave field is thus acquired before reaching North America, and care must be taken when attributing it to structure within the array. Composite maps also show the evolution of arrival-angle anomaly patterns inside the array. This is the result of velocity structure in North America, and may be attributable to specific velocity anomalies.

Predictions of arrival-angle anomalies from models S362ANI and GDM52 display the general characteristics of the observed arrival-angle anomaly patterns. Measurements of synthetic waveforms calculated using SPECFEM produce the most realistic patterns, though none of the methods or models produces the full range of deviations or the complex variations in the pattern. The phase-velocity structure in GDM52 produces better predictions of the observed anomalies than model S362ANI. Including the anisotropy in GDM52 improves the mean arrival-angle anomaly for the array, with small changes in the anomaly pattern. Including crustal structure at high resolution is important for reproducing the type of strong narrow bands of anomalies seen in the data. The comparisons indicate that current global models contain the necessary structure to produce the long-wavelength patterns in the observed arrival-angle anomalies, but not the small-scale velocity anomalies necessary to replicate the observed arrival-angle deviations. Comparisons with full synthetics are needed to use small-scale arrival-angle anomaly agreement as a benchmark for model fidelity.

Acknowledgements

We are grateful to everyone involved in the deployment and operation of USArray. The consistent and high quality of the data from the array made the research here possible. We also thank the IRIS DMC for providing simple and efficient access to these data. We thank Editor Peter Shearer, an anonymous Guest Editor, an anonymous reviewer, and Gabi Laske for helpful comments on the manuscript. This research was supported by the EarthScope Program of the National Science Foundation, grant EAR-0952285.

References

Baker, G.E., Stevens, J.L., 2004. Backazimuth estimation reliability using surface wave polarization. Geophys. Res. Lett. 31, L09611.

Bassin, C., Laske, G., Masters, G., 2000. The current limits of resolution for surface wave tomography in North America. Eos Trans. AGU 81, F897.

Bungum, H., Capon, J., 1974. Coda pattern and multipath propagation of Rayleigh waves at NORSAR. Phys. Earth Planet. Inter. 9, 111–127.

De Cacqueray, B., Roux, P., Campillo, M., Catheline, S., Boue, P., 2011. Elastic-wave identification and extraction through array processing: An experimental investigation at the laboratory scale. J. Appl. Geophys. 74, 81–88.

Dziewonski, A.M., Woodward, R., 1992. Acoustic imaging at the planetary scale. In: Emert, H., Jarges, H.-P. (Eds.), Acoustic Imaging at the Planetary Scale. In: Acoustical Imaging, vol. 19. Plenum, New York, pp. 785–797.

Dziewonski, A.M., Chou, T.-A., Woodhouse, J.H., 1981. Determination of earthquake source parameters from waveform data for studies of global and regional seismicity. J. Geophys. Res. 86, 2825–2852.

Ekström, G., 2011. A global model of Love and Rayleigh surface wave dispersion and anisotropy, 25–250 s. Geophys. J. Int. 187, 1668–1686.

Ekström, G., Busby, R.W., 2008. Measurements of seismometer orientation at USArray Transportable Array and Backbone stations. Seismol. Res. Lett. 79 (4), 554–561.

Ekström, G., Tromp, J., Larson, E.W.F., 1997. Measurements and global models of surface wave propagation. J. Geophys. Res. 102 (B4), 8137–8157.

Ekström, G., Nettles, M., Dziewonski, A.M., 2012. The global CMT project 2004–2010: Centroid-moment tensors for 13,017 earthquakes. Phys. Earth Planet. Inter. 200–201, 1–9.

Flinn, E.A., 1965. Signal analysis using rectilinearity and direction of particle motion. Proc. IEEE 53, 1874–1876.

Foster, A., Ekström, G., Nettles, M., 2014. Surface-wave phase velocities of the western United States from a two-station method. Geophys. J. Int. 196 (2), 1189–1206. http://dx.doi.org/10.1093/gji/ggt454.

Grünewald, M., 1988. Effects of anisotropy in southwest Germany on the propagation of surface waves. Phys. Earth Planet. Inter. 51, 42–54.

Jackson, G.M., Mason, I.M., Greenhalgh, S.A., 1991. Principal component transforms of triaxial recordings by singular value decomposition. Geophysics 56, 528–533.

Ji, C., Tsuboi, S., Komatitsch, D., Tromp, J., 2005. Rayleigh-wave multipathing along the west coast of North America. Bull. Seismol. Soc. Am. 95 (6), 2115–2124.

Jurkevics, A., 1988. Polarization analysis of three-component array data. Bull. Seismol. Soc. Am. 78 (5), 1725–1743.

Komatitsch, D., Tromp, J., 2002a. Spectral-element simulations of global seismic wave propagation – I. Validation. Geophys. J. Int. 149 (2), 390–412.

Komatitsch, D., Tromp, J., 2002b. Spectral-element simulations of global seismic wave propagation – II. 3-D models, oceans, rotation, and self-gravitation. Geophys. J. Int. 150 (1), 303–318.

Komatitsch, D., Vilotte, J.P., 1998. The spectral-element method: an efficient tool to simulate the seismic response of 2D and 3D geological structures. Bull. Seismol. Soc. Am. 88 (2), 368–392.

Kustowski, B., Ekström, G., Dziewoński, A.M., 2008. Anisotropic shear-wave velocity structure of the Earth's mantle: A global model. J. Geophys. Res. 113, B06306. http://dx.doi.org/10.1029/2007JB005169.

Larson, E.W.F., Ekström, G., 2002. Determining surface wave arrival angle anomalies. J. Geophys. Res. 107 (B6). http://dx.doi.org/10.1029/2000JB000048.

Larson, E.W.F., Tromp, J., Ekström, G., 1998. Effects of slight anisotropy on surface waves. Geophys. J. Int. 132, 654–666.

Laske, G., 1995. Global observation of off-great-circle propagation of long-period surface waves. Geophys. J. Int. 123, 245–259.

Laske, G., Masters, G., 1996. Constraints on global phase velocity maps from long-period polarization data. J. Geophys. Res. 101 (B7), 16059–16075.

Laske, G., Masters, G., 1998. Surface-wave polarization data and global anisotropic structure. Geophys. J. Int. 132, 508–520.

Laske, G., Masters, G., Zürn, W., 1994. Frequency-dependent polarization measurements of long-period surface waves and their implications for global phase-velocity maps. Phys. Earth Planet. Inter. 84, 111–137.

Lay, T., Kanamori, H., 1985. Geometric effects of global lateral heterogeneity on long-period surface wave propagation. J. Geophys. Res. 90 (B1), 605–621.

Lerner-Lam, A.L., Park, J.J., 1989. Frequency-dependent refraction and multipathing of 10–100 second surface waves in the Western Pacific. Geophys. Res. Lett. 16 (6), 527–530.

Levshin, A., Berteussen, K.-A., 1979. Anomalous propagation of surface waves in the Barents Sea as inferred from NORSAR recordings. Geophys. J. R. Astron. Soc. 56, 97–118.

Lin, F.-C., Ritzwoller, M.H., 2011. Helmholtz surface wave tomography for isotropic and azimuthally anisotropic structure. Geophys. J. Int. 186, 1104–1120.

Masters, G., Priestley, K.F., Gilbert, F., 1984. Observations of off-path propagation on horizontal component low frequency seismograms. Terra Cogn. 4, 250.

Montalbetti, J.F., Kanasewich, E.R., 1970. Enhancement of teleseismic body phases with a polarization filter. Geophys. J. R. Astron. Soc. 21, 119–129.

Paulssen, H., Levshin, A.L., Lander, A.V., Snieder, R., 1990. Time- and frequency-dependent polarization analysis: anomalous surface wave observations in Iberia. Geophys. J. Int. 103, 483–496.

Peter, D., Komatitsch, D., Luo, Y., Martin, R., Le Goff, N., Casarotti, E., Le Loher, P., Magnoni, F., Lui, Q., Blitz, C., Nissen-Meyer, T., Basini, P., Tromp, J., 2011. Forward and adjoint simulations of seismic wave propagation on fully unstructured hexahedral meshes. Geophys. J. Int. 186 (2), 721–739.

Ruud, B.O., Husebye, E.S., Ingate, S.F., Christoffersson, A., 1988. Event location at any distance using seismic data from a single, three-component station. Bull. Seismol. Soc. Am. 78 (1), 308–325.

Selby, N.D., 2001. Association of Rayleigh waves using backazimuth measurements: Application to Test Ban verification. Bull. Seismol. Soc. Am. 91 (3), 580–593.

Takahashi, T., 1995. Prestack migration using arrival angle information. Geophysics 60 (1), 154–163.

Tanimoto, T., Prindle, K., 2007. Surface wave analysis with beamforming. Earth Planets Space 59, 453–458.

Tromp, J., Komatitsch, D., Hjörleifsdóttir, V., Li, Q., Zhu, H., Peter, D., Bozdag, E., McRitchie, D., Friberg, P., Trabant, C., Hutko, A., 2010. Near real-time simulations of global CMT earthquakes. Geophys. J. Int. 183 (1), 381–389.

Vidale, J.E., 1986. Complex polarization analysis of particle motion. Bull. Seismol. Soc. Am. 76 (5), 1393–1405.

Woodhouse, J.H., Wong, Y.K., 1986. Amplitude, phase and path anomalies of mantle waves. Geophys. J. R. Astron. Soc. 87, 753–773.

Yoshizawa, K., Yomogida, K., Tsuboi, S., 1999. Resolving power of surface wave polarization data for higher-order heterogeneities. Geophys. J. Int. 138, 205–220.

Zywicki, D.J., Rix, G.J., 2005. Mitigation of near-field effects for seismic surface wave velocity estimation with cylindrical beamformers. J. Geotech. Geoenviron. Eng. 131 (8), 970–977.

Please cite this article in press as: Foster, A., et al. Arrival-angle anomalies across the USArray Transportable Array. Earth Planet. Sci. Lett. (2014), http://dx.doi.org/10.1016/j.epsl.2013.12.046